Conditions of inertial-viscous transition and related jetting in large cavity collapse

D. Krishna Raja,[1] E. J. Hopfinger,[2] and S. P. Das [1,*]
[1]*Department of Mechanical Engineering, Indian Institute of Technology Madras, Chennai 600036, India*
[2]*LEGI, CNRS/UGA, 38058 Grenoble Cedex 9, France*

(Received 12 June 2020; accepted 4 November 2020; published 3 December 2020)

In this paper, we present results on the effect of viscosity and surface tension on the collapse of large cavities produced by overdriving Faraday waves in a cylindrical container. The forcing amplitude of the container excitation has been increased at a rate such that the last stable wave amplitude b was close to b_s, referred to as the singular wave amplitude. The collapse of the wave-depression cavity that follows $b \lessapprox b_s$ gives rise to the largest surface jet velocities; when $b > b_s$, cavity collapse occurs with a bubble pinch-off. Viscosity has been varied by two orders of magnitude using water and glycerine-water (GW) solutions. Surface tension effects are highlighted by comparing with previously obtained results with FC 72, a low-surface-tension and low-viscosity liquid. The main objective has been to clarify how these fluid properties affect the cavity shape and cavity collapse dynamics. It is shown that the initial cavity depth depends only weakly on fluid properties, whereas the initial radius decreases with increasing viscosity and increases with decreasing surface tension. The collapse of the cavity is initially inertial with minimum cavity radius r_m varying with time in the form $r_m \sim \tau^\alpha$, with $\alpha \simeq 0.5$, where $\tau = (t_0 - t)$, with t_0 being the time at singular collapse. In high-viscosity fluids, there is an inertial-viscous transition to $\alpha = 1$, whereas in water the transition is to $\alpha > 1/2$ and is close to $2/3$, indicating an inertial-capillary transition. In low-viscosity and low-surface-tension fluid (FC 72), collapse remains inertial up to singular collapse. The transitions are characterized by the evolution of the relevant dimensionless flow parameters. It is shown that inertial-viscous transition occurs when the capillary number, $\mathrm{Ca} = U_r\mu/\sigma$, defined with the local radial velocity, U_r, changes from $\mathrm{Ca} < 1$ to $\mathrm{Ca} > 1$, while the local Ohnesorge number is large, $\mathrm{Oh} = \mu/\sqrt{\rho\sigma r_m} \gtrsim 0.1$. The local Reynolds number at transition remains large and decreases with decreasing τ to $\mathrm{Re} \sim 1$. The velocity of the jet, emerging from the free surface following singular collapse, increases with viscosity, and reaches a maximum in GW. Numerical simulations give an indication of the increase and localization of the pressure that drives the liquid jet with a high-speed precursor air jet.

DOI: 10.1103/PhysRevFluids.5.124002

I. INTRODUCTION

Cavity formation and its subsequent collapse with related jetting is a frequently encountered event. It is observed when objects enter or exit from a liquid surface [1,2] or when axisymmetric wave-depression cavities collapse [3–7]. At a smaller scale, similar phenomena are observed in surface bubble bursting [8–13]. In this case the collapse is surface tension driven with a viscous cutoff at large Ohnesorge number, $\mathrm{Oh}_c > 0.037$ [11,12,14]. On the contrary, in the collapse of wave-depression cavities or cavities formed by objects, of the size of order 1 cm or larger, inertia

*spdas@iitm.ac.in

is dominant. Inertia-driven cavity collapse can lead to finite-time singularities and high-velocity jets as has been demonstrated in experiments by Zeff *et al.* [4], Das and Hopfinger [5], and Raja *et al.* [6,7], where the cavities have been created by overdriving a subharmonically forced standing wave in a cylindrical container up to the desired last stable wave amplitude b that precedes collapse of the following wave-depression cavity. When this wave amplitude is less than the critical wave amplitude b_s, referred to as singular wave amplitude [4], the domain remains simply connected during cavity collapse and jet initiation. When the wave amplitude is driven to a height beyond this singular wave amplitude, i.e., to $b > b_s$, cavity pinch-off occurs so that the domain becomes multiply connected. Such multiply connected topologies are also observed in free surface bubble collapse [11,13], disk impact [1], or drop impact processes [15,16]. In large-viscosity fluids the collapse process is regularized by damping of any perturbations, hence leading to greater critical wave amplitudes [7], and following smaller cavity radii.

Longuet-Higgins and Oguz [17] derived a power-law dependence of cavity radius r on time of the form $r \sim \tau^{\alpha}$, where $\tau = (t_0 - t)$, with t_0 being the time at singular collapse (jet initiation). The exponent α, in their theory, is asymptotically limited to 2/3 with the lower value close to 0.5. The exponent 2/3 is observed in bubble bursting [10,18], whereas in collapse of a giant bubble, created by a moving disk [1], α approaches 1/2 with increasing disk Froude number. The radial collapse of cavities generated by drop impact on liquid pool also follows a similar power law with an exponent $\alpha \approx 1/2$ [16]. During wave-depression cavity collapse in viscous fluids, Raja *et al.* [6] showed that the minimum cavity radius decreases with time with an exponent $\alpha \approx 0.5$ with a transition to a larger exponent, when the cavity radius approaches the singular radius at time t_0. In fluids of high viscosity the exponent α increases to $\alpha \simeq 1$ with the inertial-viscous transition taking place at $\mathrm{Ca} = U_r\mu/\sigma \approx 1$ [7]. Similarly, in numerical simulations of the contraction of a small hole in a fluid sheet, Lu and Corvalan [19] showed an inertial-viscous transition that occurs at a local capillary number $\mathrm{Ca} \sim 1$. An inverse, viscous-inertial transition, from $\alpha = 1$ to $\alpha = 0.5$, has been identified by Burton and Taborek [20] in the coalescence of two, initially circular, lenses.

Concerning jetting, in the experiments by Raja *et al.* [6] jet velocities as high as 50 m/s have been measured in water with 1% detergent added. Measured jet velocities have also been shown to agree well with a finite-time singularity scaling as first proposed by Zeff *et al.* [4]. In distilled water, Das and Hopfinger [5] measured jet velocities that are less than in water with 1% detergent, although the fluid properties are practically the same. In FC 72 (perfluorohexane, C_6F_{14}) which is an electronic coolant liquid generally used for low-temperature heat transfer applications, considerably lower jet velocities have been observed, with the jet being irregular [5]. In high-viscosity fluids, jet velocities of 100 m/s and more have been measured by Raja *et al.* [7] that are associated with cusp formation at singular collapse.

There is an incentive for clarifications of the effects of viscosity and also surface tension on inertial-viscous transition and/or inertial-capillary transition as well as on cavity shapes. In the present experiments, fluids of widely different viscosity are considered. Surface tension effects are discussed with respect to results previously obtained by Das and Hopfinger [5] with FC 72. Cavity collapse and inertial-viscous or inertial-capillary transitions are characterized by determining the different dimensionless flow parameters governing collapse. The present experiments focus on conditions where the subharmonic forcing is chosen such that the last stable wave amplitude $b \lessapprox b_s$ at which the jet velocities are largest. In Sec. II the experimental methods and the conditions are discussed. The results are presented in Sec. III, where the cavity shapes are first discussed, followed by the collapse dynamics and effect of viscosity and surface tension on jet velocity. The conclusions are presented in Sec. IV.

II. EXPERIMENTAL METHODS AND CONDITIONS

The experiments have been conducted in a container similar to that used by Raja *et al.* [6] with fluids at room temperature, generally around 25°C and widely different viscosities. A schematic diagram of the experimental set-up is shown in Fig. 1. A circular, cylindrical container, made

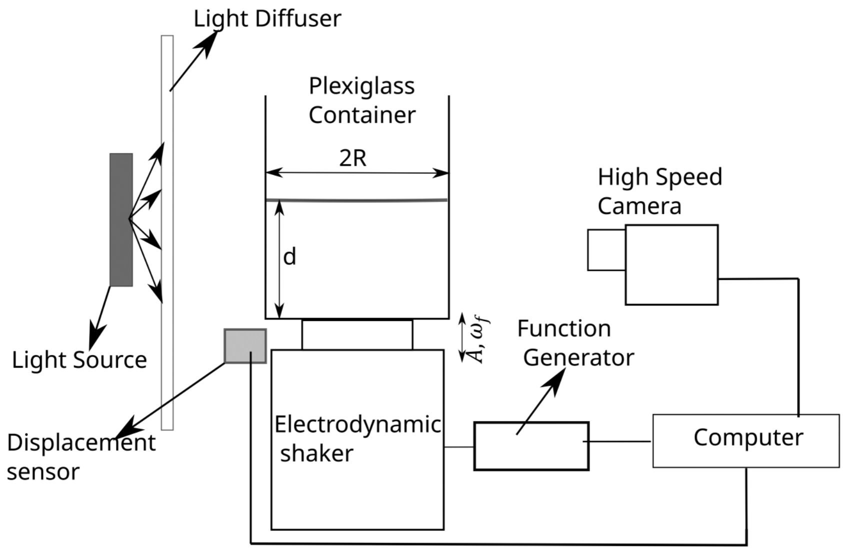

FIG. 1. Experimental setup consisting of function generator, electrodynamic shaker, and the imaging facility. The imaging facility includes a light source, light diffuser, and a high-speed camera. A function generator is used to control the shaker and displacement sensor to measure the shaker response.

of Plexiglas, of diameter $2R = 10 \pm 0.04$ and 10 cm deep is mounted on a vertically oscillating vibrator APS 400 ELECTRO-SEIS of peak force 440 N. After calibration, the vibration amplitude was controlled within 0.30% of the nominal value and the frequency within 0.02%. Since the forcing is normal to the fluid surface, the waves are subharmonically excited. The fluid depth to radius ratio was $d/R = 1.2$, which is sufficient to satisfy deep-water conditions for the axisymmetric mode [21] with $\tanh(k_{01}d) \approx 1$, where k_{01} is the wave number of the lowest axisymmetric mode. The container acceleration in present experiments is given by $a(t) = A\omega_f^2 \sin(\omega_f t)$, with $a \leqslant 6$ m/s^2, where ω_f is the forcing frequency, equal to twice the wave frequency ω, and A the forcing amplitude. Measurements were made by visualizations and image analysis. A high-speed camera with an acquisition speed of 2000–8000 frames per second was used.

The experiments are performed in a controlled environment to limit surface contamination from the atmosphere. The container used for experiments is cleaned and dried properly. Also, distilled water is used for the experiments and for preparing the different glycerin-water solutions. The surface tension is measured in the laboratory using tensiometer with collected samples of the working fluid. The properties of the fluids used, water and glycerin-water solutions (GW solutions), are given in Table I, together with the stability threshold forcing amplitude A_c/R. The corresponding frequency is $\omega_0 = \omega_{01}(1 - \delta)$, where δ is the damping coefficient [21], with natural frequency ω_{01} given by the dispersion relation [22],

$$\omega_{mn}^2 = gk_{mn}\left(1 + \frac{k_{mn}^2\sigma}{g\rho}\right)\tanh(k_{mn}d), \tag{1}$$

where the wave mode (m, n) expresses m nodal diameters and n nodal circles with $m = 0, 1, \ldots$ and $n = 1, 2, \ldots$. For wave growth leading to wave breaking, it is necessary to overdrive the wave motion with an amplitude $A > A_c$, where A_c is the forcing amplitude stability threshold. Experiments have been conducted at $\omega/\omega_0 = 0.995$ by increasing A/R at a rate such that the last stable wave amplitude $b \lessapprox b_s$, the singular wave amplitude.

Figure 2 shows the definitions of the variables used, with b the last stable wave amplitude, Z_c the corresponding wave-depression cavity depth, and its radius r_i. The initial cavity shape is

TABLE I. Fluid properties at 25°C and experimental conditions. The suffix numbers of GW refer to the percentage by volume of glycerine in water. A_c is the stability threshold forcing amplitude and A the forcing amplitude that gives final wave amplitude b close to b_s, the singular wave amplitude.

Fluid	ρ (g/cm^3)	ν (cm^2/s)	σ (dyne/cm)	A_c/R ($\omega/\omega_0 = 1$)	A/R ($\omega/\omega_0 = 0.995$)	b_s/R
Water (distilled)	1.000	0.010	72.0	0.0056	0.020	0.936
GW 60	1.160	0.090	67.0	0.0062	0.022	0.990
GW 80	1.205	0.500	64.0	0.0130	0.027	1.002
GW 90	1.230	2.160	63.4	0.0215	0.032	1.027
FC 72[a]	1.680	0.004	11.0	0.0010	0.010	0.880

[a]Conditions for FC 72 (perfluorohexane, C_6F_{14}), which is an electronic coolant liquid of low surface tension and low viscosity taken from Das and Hopfinger [5].

characterized by radius r_i and Z_c, the wave-depression cavity depth, when cavity collapse starts (beginning of radial shrinkage of the cavity). The final cavity shape (radius r_0 and depth Z_0) is the shape of cavity recorded one frame before jet formation, i.e., rapid vertical shrinkage of the cavity. The changes with time τ of cavity depth and radius are denoted by Z and r_m, where $\tau = (t_0 - t)$ with t_0 the time when the cavity reaches the singular radius r_0 with depth Z_0. The radius of the jet r_j is measured when the jet emerges above the free surface.

III. RESULTS AND DISCUSSION

A. Cavity shapes

The initial cavity depths Z_c and radius r_i are presented as a function of dimensionless viscosity, $\nu/\sqrt{R^3 g} = 1/\mathrm{Re}_I$ in Fig. 3, where $\mathrm{Re}_I = (\sqrt{R^3 g}/\nu)$ is a Reynolds number defined with the inertial velocity scale $\sqrt{Rg}$. Results obtained with FC 72, taken from Das and Hopfinger [5], are included for comparison. This is of interest because its kinematic surface tension σ/ρ is 10 times less than that of water while the kinematic viscosity is of the same order. It is seen from Fig. 3 that the

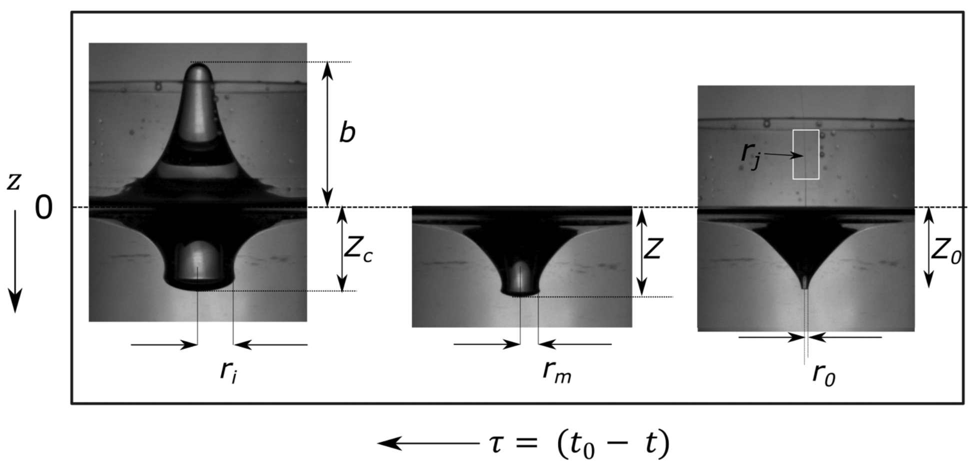

FIG. 2. Definitions of Z_c, r_i, r_0, r_j, and Z_0, where Z_c is the depth and r_i the corresponding radius of the full-grown wave-depression cavity formed by the last stable wave amplitude b. r_m and Z are the minimum radius and depth at any instant τ. r_j is the radius of the jet when it emerges at the free surface. The dotted horizontal line at $z = 0$ represents the unperturbed free surface.

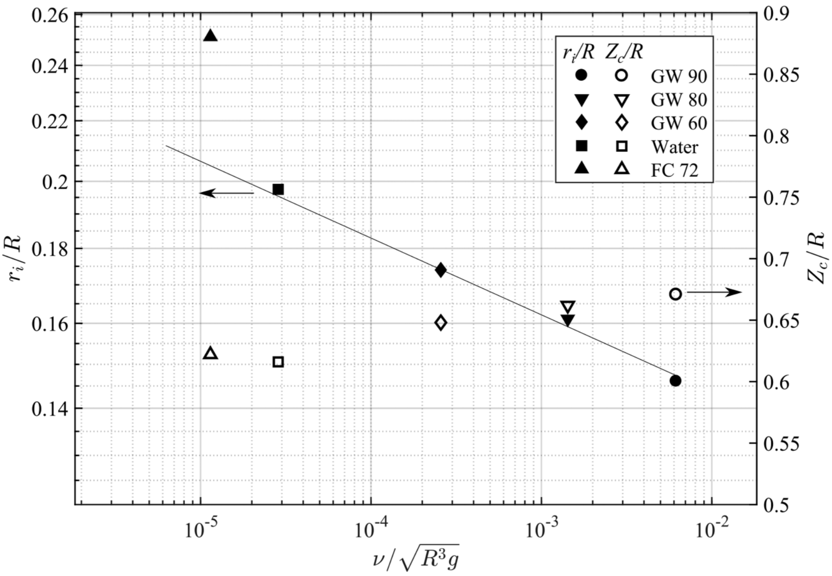

FIG. 3. Initial radius r_i/R (the left y axis) and depth Z_c/R (right y axis) of cavity as a function of dimensionless viscosity $\nu/\sqrt{R^3 g}$. The filled symbols correspond to the initial cavity radius (left y axis, $\longleftarrow$) and the open symbols indicate the depth, (right y axis $\longrightarrow$). The solid line indicates $r_i/R \propto \nu/\sqrt{R^3 g}$ when surface tension (σ) is nearly constant.

initial cavity radius decreases by about 30% when the viscosity is increased by a factor of 10^2 while the cavity depth increases by less than 10%. In FC 72 that has somewhat lower viscosity than water but much lower kinematic surface tension σ/ρ, the cavity depth is slightly less but the cavity radius is noticeably larger. The last stable wave amplitude is also lower and is more irregular (see Das and Hopfinger [5]) because inertia is largely dominating over surface-tension and viscosity effects.

In Fig. 4, images of the different cavity shapes in water [Fig. 4(a)], GW 80 [Fig. 4(b)], and GW 90 [Fig. 4(c)] are presented, with the left column showing the initial cavity shapes, r_i and Z_c, and the middle column the singular states, r_0 and Z_0. As expected, the cavity boundaries are smoother in GW than in water, especially at the singular state as is clearly seen in the enlarged view of the cavity tip region (right column of Fig. 4). In water the cavity boundary has an irregular shape with perturbations in the form of capillary waves which results in rupture at a larger r_0.

The wavelength that is damped by viscosity can be evaluated from linear theory [23] of internal damping rate $\kappa = 2\nu k^2$, where k is the wave number. Krishnan *et al.* [11] showed that this damping rate is a good approximation for damping of small amplitude capillary waves on the cavity boundary of bubble bursting in water as well as in glycerine water. Raja *et al.* [6] considered a decay rate $\kappa = C\nu k^2$ showing that wavelengths

$$\frac{\lambda}{R} \leqslant 3.98\sqrt{\frac{C}{\mathrm{Re}_I}} \tag{2}$$

will be damped, where $C \simeq 2$ has been experimentally determined for capillary waves in water. With $C = 2$ [6,24], capillary waves of wavelength of about the cavity depth are damped in a container $2R = 10$ cm and fluid viscosity $\nu = 1$ cm^2/s. The wavelengths that are damped are indicated in Fig. 5 for water [Fig. 5(a)], GW 80 [Fig. 5(b)], and GW 90 [Fig. 5(c)]. In GW 90, wavelength of the order of the cavity depth are damped indicating a smooth boundary as shown in Fig. 5(c),

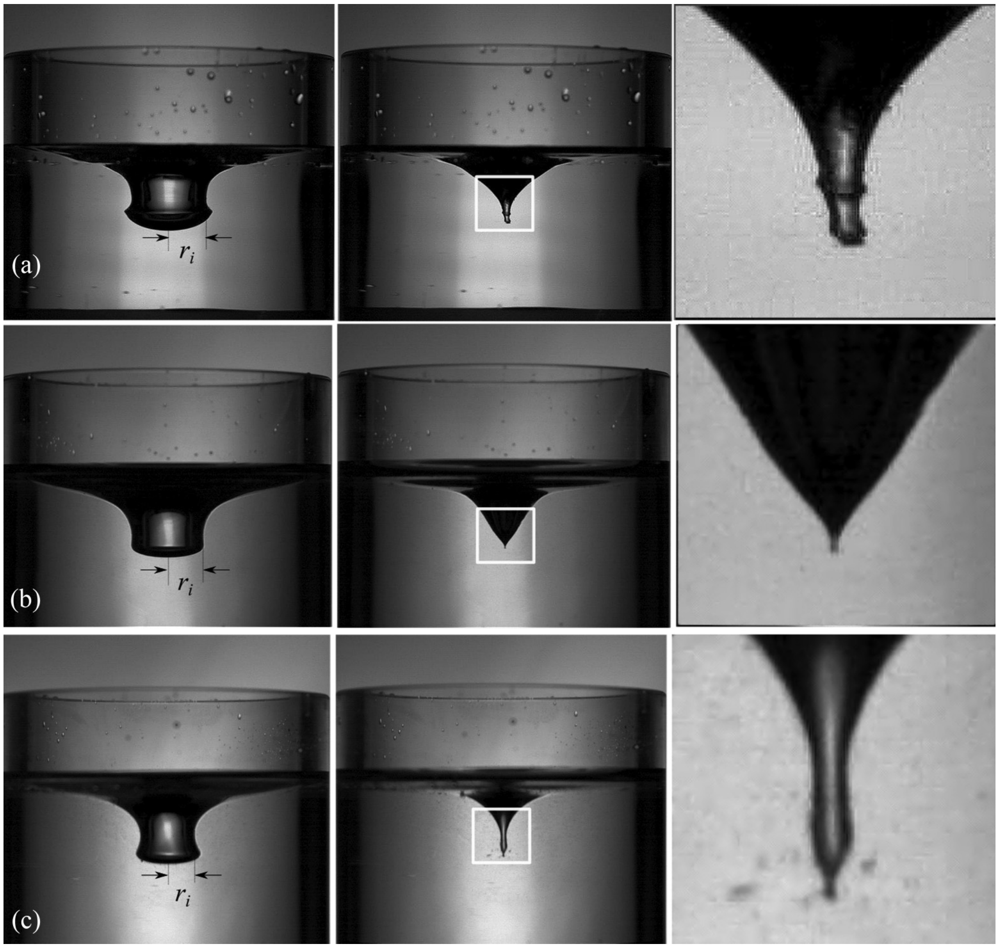

FIG. 4. Stages of cavity collapse (from left to right): Full-grown cavity radius, r_i, final cavity radius, r_0, and enlarged views at final collapse. (a) Water, $b_s/R = 0.936$, $\lambda/R = 0.03$; (b) GW 80, $b_s/R = 1.002$, $\lambda/R = 0.213$; (c) GW 90, $b_s/R = 1.027$ with $\lambda/R = 0.44$.

whereas in water as shown in Fig. 5(a), perturbations of less than the cavity radius are damped [see also Fig. 4(a), right column] and in GW 80 wavelengths $\lambda/R \approx 0.25$ are damped. The calculated wavelengths are indicated by vertical lines in Fig. 5.

FIG. 5. Cavity shapes at $\tau = 1$ ms (a) water, (b) GW 80, and (c) GW 90. The calculated wavelengths λ are indicated by the vertical lines. The dotted horizontal lines in (a) shows the measured wavelength.

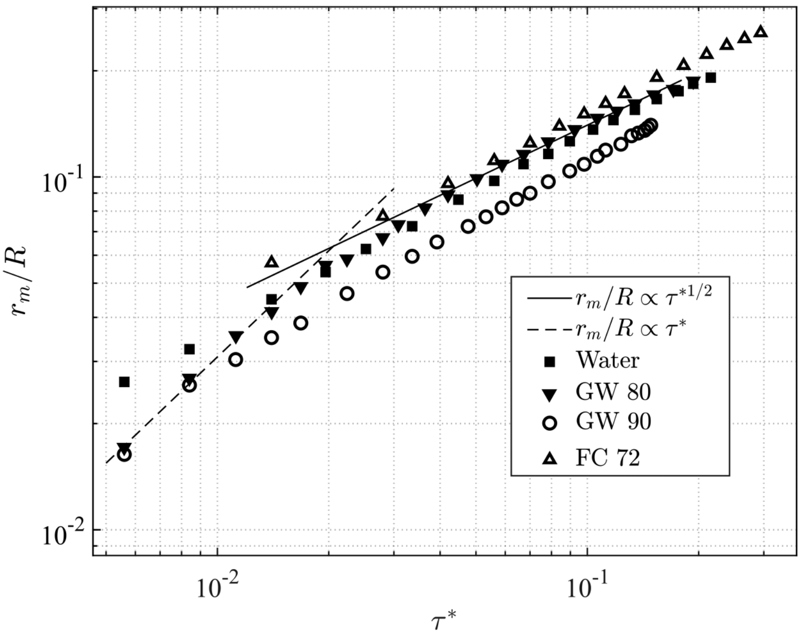

FIG. 6. Minimum cavity radius r_m/R as a function of dimensionless time $\tau^* = \tau/\sqrt{R/g}$. The symbols ■, ▼, and ○ represent water, GW 80, and GW 90, respectively. FC 72 (△) data have been taken from Das and Hopfinger [5]. The solid and dashed lines correspond to $r_m/R \propto \tau^{*1/2}$ and $r_m/R \propto \tau^*$, respectively.

B. Cavity collapse dynamics

The rate of change of cavity radius is shown in Fig. 6 where the cavity radius r_m/R is plotted as a function of the dimensionless time $\tau^* = \tau/\sqrt{R/g}$ for the fluids with widely varying viscosity. Water and GW 80 exhibit at the beginning of collapse a clear inertial regime of $r_m/R \propto \tau^{*^{\alpha}}$, with $\alpha \simeq 1/2$. As the singular collapse is approached, the exponent in GW 80 changes to $\alpha \simeq 1$, characteristic of a viscous regime. In water, no viscous regime is approached with the final slope being closer to $\alpha \simeq 2/3$ indicating a capillary regime. Experiments in water with added detergent seemed to suggest an inertial-viscous transition [6]. This misinterpretation was due to the low camera speed available for these experiments. The intermediate regime spans half a decade in τ^*, which is about one-third of the total time span of cavity collapse. The time dependency of the cavity radius in GW 90 is mostly in an intermediate regime of $\alpha > 1/2$, indicating that collapse is affected by viscosity from the beginning, with a change to a clear viscous regime $\alpha \simeq 1$ near the singular collapse. In FC 72, the available data indicates an inertial collapse over the whole time span. There exists no data very close to the singular radius, but since the kinematic viscosity and the kinematic surface tension are much lower than in water, no viscous or capillary effects are expected.

Assuming the cavity collapse to be spherically symmetric of radius r_m close to the cavity base (during collapse, the minimum radius location moves toward the cavity tip) and using the analytical approximate solution of Duclaux *et al.* [25], the equation of collapse can be written in dimensionless form as:

$$\frac{d^2 r_m^{*2}}{d\tau^{*2}} + \left(\frac{dr_m^*}{d\tau^*}\right)^2 = -2Z^* + \frac{1}{\mathrm{Bo}_R\, r_m^*} + \frac{2}{\mathrm{Re}_I}\frac{1}{r_m^*}\frac{dr_m^*}{d\tau^*}, \tag{3}$$

where $r_m^* = r_m/R$ and $\tau^* = \tau/\sqrt{R/g}$ with length scale R and the characteristic time $\sqrt{R/g}$. The cavity is initially at rest and driven radially by the hydrostatic pressure. The first term in left-hand side is balanced by the first term of right-hand side. The last two terms on the right-hand side

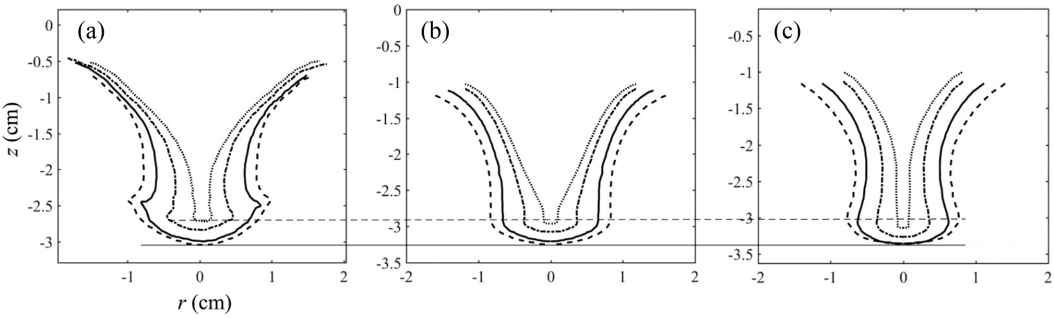

FIG. 7. Cavity shapes at times $\tau^* = 0.0056,\ 0.028,\ 0.084$, and 0.14. (a) Water, (b) GW 80, and (c) GW 90. The horizontal solid and dotted lines indicate respectively $z = Z_c$ and final cavity depth $z = Z_0$ in water.

of Eq. (3) are at least two orders of magnitude less than Z^* because $\mathrm{Bo}_R = \rho g R^2/\sigma$ and $\mathrm{Re}_I = R\sqrt{Rg}/\nu$ are large and r_m^* is finite. This is similar to the equation (4.10) of Duclaux *et al.* [25] with solution $r_m^* \sim (4r_i^2 g Z_c)^{1/4}\tau^{*1/2}$. In the late stages of collapse, viscous and capillary forces become important. It is seen from experiments that the velocity becomes nearly constant close to collapse; hence, the first term of left-hand side can be neglected. For low-viscosity fluids like water, the inertia is then balanced by the capillary force, which gives an inertial-capillary transition with a crossover from $\tau^{*1/2}$ to $\tau^{*2/3}$. In fluids of high viscosity like GW 80, when $r_m \to 0$, the viscous term is equal or larger than the capillary term which gives $r_m^* \lesssim \tau^*/\mathrm{Ca}_R$, where $\mathrm{Ca}_R = \mu\sqrt{Rg}/\sigma$. In order to highlight the inertial-viscous transition with respect to inertial-capillary transition, cavity contours at different times are presented in Fig. 7 for water and GW. In water [Fig. 7(a)], the cavity boundary has a pronounced kink at the curvature change which persists up to the singular radius. This is indicative of dominant capillary forces so that no inertial-viscous transition is expected. In GW the cavity boundary is more cylindrical, and the cavity base has practically no curvature; the lower part of the cavity looks more like a cylindrical tube (see also Fig. 5). The radial velocity of cavity collapse is shown in Fig. 8 as a function of τ^*. In the beginning, the radial velocity is small (the radial velocity is zero just before Z_c is reached) and then the cavity boundary of radius r_m is accelerated inward by the base pressure $\rho g Z_m$. Here Z_m is the depth corresponding to r_m, the location of which depends on the cavity shape. It moves toward the cavity tip during collapse. The inward

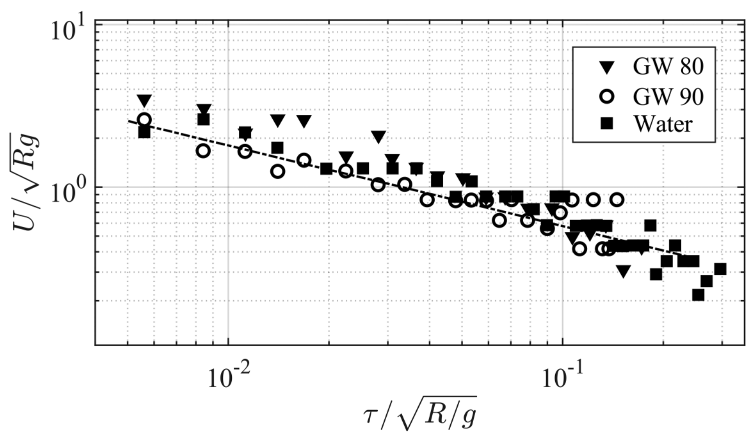

FIG. 8. Measured radial velocity $U_r/\sqrt{Rg}$ as a function of time. The symbols ■, ▼, and ○ represent water, GW 80, and GW 90, respectively. The dashed line is $-1/2$ slope corresponding to $r_m \sim \tau^{1/2}$.

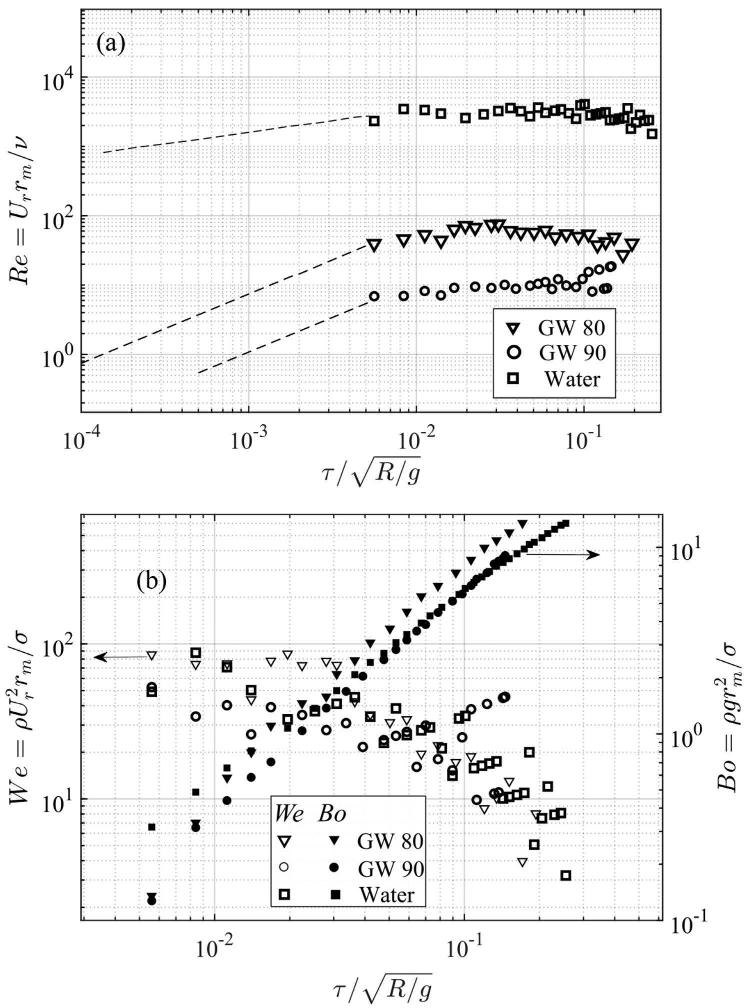

FIG. 9. (a) Reynolds number $\mathrm{Re} = U_r r_m/\nu$ as a function of dimensionless time $\tau/\sqrt{Rg}$, with the dashed lines representing the expected decrease of Re with decreasing $\tau/\sqrt{Rg}$. (b) Weber number $\mathrm{We} = \rho U_r^2 r_m/\sigma$ and Bond number $\mathrm{Bo} = \rho g r_m^2/\sigma$ as a function of dimensionless time. The symbols ○, ∇, and □ are, respectively, GW 90, GW 80, and water. The open symbols correspond to We (left y axis $\longleftarrow$) and filled symbols indicate Bo (right y axis $\longrightarrow$).

velocity increases with decreasing radius and is larger in GW as the singular collapse is approached, in accordance with the rate of radial cavity change shown in Fig. 6.

In Fig. 9, local Reynolds [Fig. 9(a)] and Weber numbers [Fig. 9(b)], calculated with U_r and r_m, are plotted as a function of τ^*. As seen in Fig. 9(a), $\mathrm{Re} = U_r\, r_m/\nu$ in water is very large and is practically constant. In GW 80, $\mathrm{Re} \lesssim 100$ at transition and decreases toward singular collapse to a value of $\mathrm{Re} \approx 50$ at $\tau^* \approx 5 \times 10^{-3}$. The experimental data points are limited by the frame rate. The value of the Reynolds number at singular collapse can be evaluated by extrapolating r_m and U_r to $\tau^* \to 0$. Figure 6 (dashed line) indicates that in the viscous regime $r_m/R \simeq 3.1\ \tau^*$ and $U_r/\sqrt{gR} \simeq 3.1$, (see Fig. 8). Hence, in GW 80 $\mathrm{Re} = U_r r_m/\nu \simeq 9.61\sqrt{gR^3}\tau^*/\nu \simeq 1$ when $\tau^* = 1.5 \times 10^{-4}$ and $\mathrm{Re} \ll 1$ when $\tau^* \to 0$. A similar extrapolation of water data gives $\mathrm{Re} \sim 10^3$. In GW 90, $\mathrm{Re} \approx 10$ at $\tau^* > 0$, indicating that viscous effects cannot be neglected from the beginning of collapse. The importance

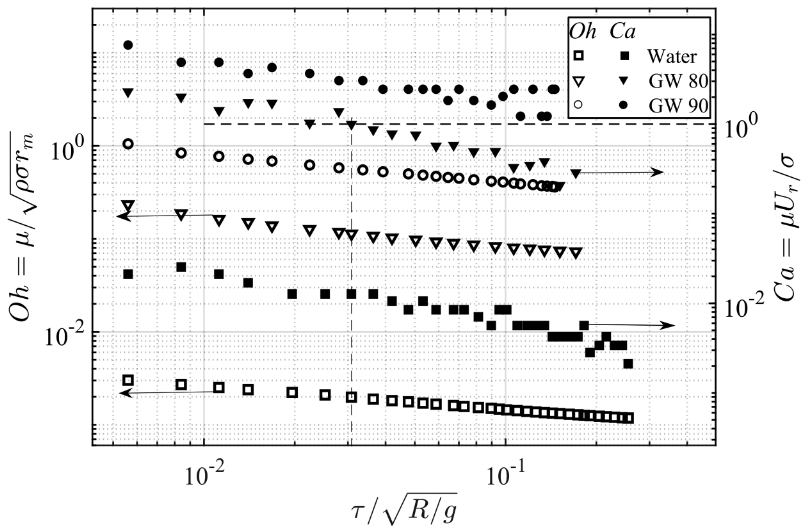

FIG. 10. Log-log plot of Oh and of Ca as a function of τ^*. Oh is indicated by open symbols with values on the left y axis $\longleftarrow$ for (□) water, (∇) GW 80, and (○) GW 90. The values of the corresponding capillary number Ca (filled symbols) are given on the right y axis $\longrightarrow$. The horizontal and vertical dashed lines respectively indicate $\mathrm{Ca} = 1$ and $\tau^* \approx 0.03$.

of capillary effects with respect to inertia is expressed by the Weber number $\mathrm{We} = \rho U_r^2 r_m/\sigma$ shown in Fig. 9(b). It increases with decreasing τ^* to a maximum 10^2 in GW and to about 50 in water. In FC 72 the Weber number is of order 10^3. The very low values of the Weber number, $\mathrm{We} < 10$, at the beginning of collapse would suggest that surface-tension forces are important. However, initially, the Bond number $\rho g r_m^2/\sigma$ also plotted in Fig. 9(b) is large, indicating that acceleration is dominant. Most informative about respective viscous and capillary effects are the capillary number, $\mathrm{Ca} = \mu U_r/\sigma$ ($\mathrm{Ca} = \mathrm{We}/\mathrm{Re}$), and $\mathrm{Oh} = \mu/\sqrt{\rho\sigma r_m}$ ($\mathrm{Oh} = \sqrt{\mathrm{We}}/\mathrm{Re}$), shown in Fig. 10 as a function of τ^*. During collapse Ca increases. In GW 80 its value at inertial-viscous transition is $\mathrm{Ca} \simeq 1$ at $\tau^* \approx 0.03$, indicated by dashed lines in Fig. 10, which corresponds to the beginning of transition from inertial regime (see Fig. 6). The capillary number reaches a value $\mathrm{Ca} \simeq 2.4$ at $\tau^* = 0.0056$ increasing further as singular collapse is approached. The corresponding Ohnesorge number is $\mathrm{Oh} \approx 0.12 > \mathrm{Oh}_c$ at transition, with $\mathrm{Oh}_c \approx 0.037$ [11,14]. In GW 90, capillary number is always greater than 1 and the inertial regime is nearly nonexistent (see Fig. 6). In water, $\mathrm{Ca} \ll 1$ and $\mathrm{Oh} \ll \mathrm{Oh}_c$ indicate that the surface tension dominates over viscosity so that the transition should be inertial-capillary. In FC 72, the Oh is close to that of water, and Ca is 5 times larger than in water but still $\mathrm{Ca} \ll 1$. This, in addition to large We and Re numbers, indicates that collapse is inertial up to singular collapse at $\tau^* = 0$.

C. Effect of viscosity and surface tension on jet velocity

The velocity of the jet that emerges at the free surface following singular cavity collapse is shown in Fig. 11 as a function of dimensionless viscosity. The jet velocity is highest in GW 80, reaching $U_j \approx 120$ m/s, with local capillary number $\mathrm{Ca} > 1$ at singular collapse and with the shape of the cavity base forming a cusp [7]. This occurs at a dimensionless viscosity $\nu/\sqrt{R^3 g} \approx 0.0014$. The emerging jet is very thin ($2r_j \approx 0.2$ mm) and straight. At larger viscosity the emerging jet is similar but of lesser velocity ($U_j \approx 87$ m/s) because there is viscous damping during jet emergence. The jet velocity would further decrease if the viscosity is increased. A decrease in viscosity also results in a lesser jet velocity, which is demonstrated by the experiments in GW 60 ($U_j \approx 63$ m/s). In

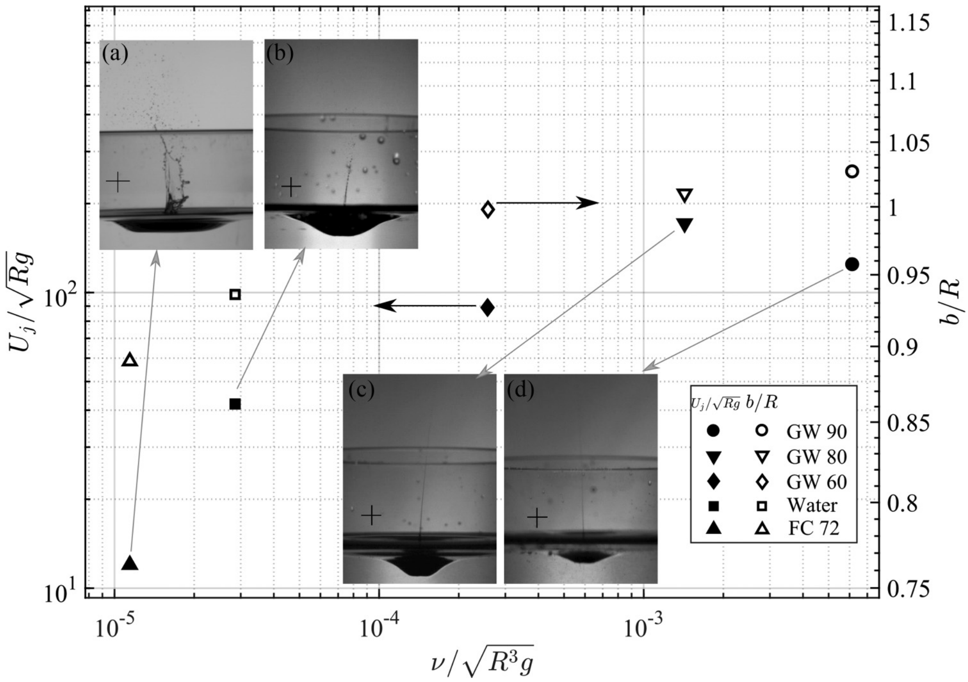

FIG. 11. Log-log plot of dimensionless jet velocity $U_j/\sqrt{gR}$, filled symbols with values on left y axis ($\longleftarrow$) and of last stable wave amplitude, b/R, open symbols (right y axis $\longrightarrow$) as a function of dimensionless viscosity $\nu/\sqrt{R^3 g}$. Insets: (a) Jet in FC 72, jet radius $r_j/R \approx 5.4 \times 10^{-2}$; (b) water, $r_j/R \approx 10^{-2}$; (c) GW 80, $r_j/R \approx 2 \times 10^{-3}$; and (d) GW 90, $r_j/R \approx 2 \times 10^{-3}$. Note that the jet images are at different time after singular collapse occurring at $\tau^* = 0$. The horizontal and vertical bars in the insets represent 1 cm.

water the singular cavity shape is parabolic, and hence jet velocity is much less with a jet diameter $2r_j \sim 1$ mm and the jet is not straight and breaks up rapidly into drops (see inset image). The jet can be straight in water but this is not generally the case. In FC 72 the jet velocity is considerably lower, which is a combined effect of very low kinematic viscosity and low kinematic surface tension. It is also seen in inset images that the jet diameter in FC 72, as it emerges at the free surface, is large ($2r_j \approx 5.4$ mm), is very irregular, and forms sheets and spray.

The last stable wave amplitude shown in Fig. 11 depends on the way the wave motion is overdriven, i.e., on forcing amplitude that depends on fluid properties. It increases with increasing viscosity and is largest at the largest viscosity which would suggest a larger jet velocity. However, as discussed above and seen in Fig. 11, the jet velocity decreases because of viscous damping of the jet. There is thus an optimal viscosity for highest jet velocity.

IV. CONCLUSION

Experiments, conducted with large cavities produced by overdriving Faraday waves in fluids of kinematic viscosity ν ranging from $\nu = 0.004$ cm^2/s to 2 cm^2/s in a cylindrical container demonstrate three distinct collapse processes: (i) In high-viscosity fluids, such as GW 80 ($\nu = 0.50$ cm^2/s), an inertial-viscous transition takes place with a time dependency of cavity radius $r_m \sim \tau^\alpha$, with $\alpha \simeq 0.5$ in the inertial regime, increasing to $\alpha \simeq 1$ toward singular collapse, indicative of a viscous regime, where $\tau = (t_0 - t)$, with t_0 being the time at singular collapse. This inertial-viscous transition occurs when the capillary number $\mathrm{Ca} = U_r\mu/\sigma$, based on the local radial velocity U_r, changes from $\mathrm{Ca} < 1$ to $\mathrm{Ca} > 1$, while the local Ohnesorge number $\mathrm{Oh} = \mu/\sqrt{\rho\sigma r_m} \approx 0.12 > \mathrm{Oh}_c$ with $\mathrm{Oh}_c \approx 0.037$ [11]. The local Reynolds number at transition is $\mathrm{Re} = U_r r_m/\nu \lesssim 100$ decreasing to

Re $<$ 1 at singular collapse; (ii) in low-viscosity fluids, here water, local Ca $\ll 1$, Oh $\ll$ Oh$_c$, and Re $\gg 100$, while the local Weber number We < 100, indicating increasing capillary effects with possible inertial-capillary transition; (iii) in fluids of low viscosity with, in addition, low kinematic surface tension such as FC 72 ($\sigma = 11$ dyne/cm and $\nu = 0.00406$ cm^2/s), collapse remains inertial up to singular collapse because the local Ca $\ll 1$, Oh $\ll$ Oh$_c$, and Re $\gg 100$, while the local Weber number is We $\sim 10^3$. Concerning the initial cavity shape, the cavity depth is only weakly dependent on fluid properties while the initial radius r_i increases with increasing surface tension and decreases with increasing viscosity. In particular, viscosity prevents perturbations in the form of capillary waves so that the cavity boundary is smooth and the cavity is axisymmetric.

The velocity of the jet that is emerging from the free surface following singular collapse increases with viscosity and reaches $U_j \approx 120$ m/s, when there is a viscous transition, as observed in GW 80. These high velocities are the result of cusp formation as has been shown by Raja *et al.* [7]. In this case, Ca > 1, Oh $>$ Oh$_c$, and Re $\rightarrow\sim 1$ as $\tau^* \rightarrow 0$. The emerging jet is very thin and straight. When the viscosity is larger such that the local capillary number is always Ca > 1, as in GW 90, viscosity has a damping effect and the jet velocity is less even though the last stable wave amplitude and following initial cavity depth are larger. In water, the jet velocity is much less, and the jet may not be straight and breaks up rapidly into droplets. In FC 72 the jet velocity is considerably lower and the jet is irregular, which is a combined effect of very low kinematic viscosity and low kinematic surface tension.

Numerical simulations conducted for conditions of GW 90, presented in the Appendix, are qualitative but demonstrate the intensity and localization of the pressure increase that drives the jet. These simulations also include the air jet, not seen in experiments, coming out from the cavity that is largest just before liquid jet formation. The interest of these simulations is to show the large pressure increase at the cavity tip.

ACKNOWLEDGMENTS

The authors thank Professor Shaikh Faruque Ali, Department of Applied Mechanics, and Professor Sabita Sarkar, Department of Metallurgical and Materials Engineering, Indian Institute of Technology Madras, for providing laboratory facilities and equipment to conduct the experiments.

APPENDIX: NUMERICAL SIMULATIONS OF CAVITY COLLAPSE

1. Numerical methodology

The numerical simulations are carried out with the aim to understand the pressure build-up and its location as well as the velocity field during cavity collapse. The simulations are performed with widely used software Ansys Fluent, which performs reasonably well in the case of free surface problems. The VOF method implemented in Fluent (explicit formulation with Geo reconstruct scheme) is able to track the sharp liquid-gas interface quite accurately. The computational domain corresponding to the experiments, is a cylindrical container of radius 5 cm and height 20 cm (10 cm in experiments). Since the cavity collapse and jet formation is axisymmetric for (0,1) mode, a two-dimensional axisymmetric domain is used for representing the cavity. Grid is generated in the domain using ICEM CFD with refined mesh sizes near the axis and the interface. Boundary conditions are no-slip on the side and the bottom walls, and a pressure boundary condition at the open top of the container. The container is excited by implementing a user-defined function that imposes the sinusoidal motion. The solution is initialized with an unperturbed free surface formed in GW 90 and air. GW 90 is chosen for the calculations because of its larger viscosity.

The time steps are chosen to limit the Courant number far below 1. The jetting and the cavity dynamics have been simulated with very small time steps of the order 10^{-6} to capture the transients as accurate as possible. Surface tension effects are included using the continuum surface force model, which considers the surface tension as a volume force at the interface.

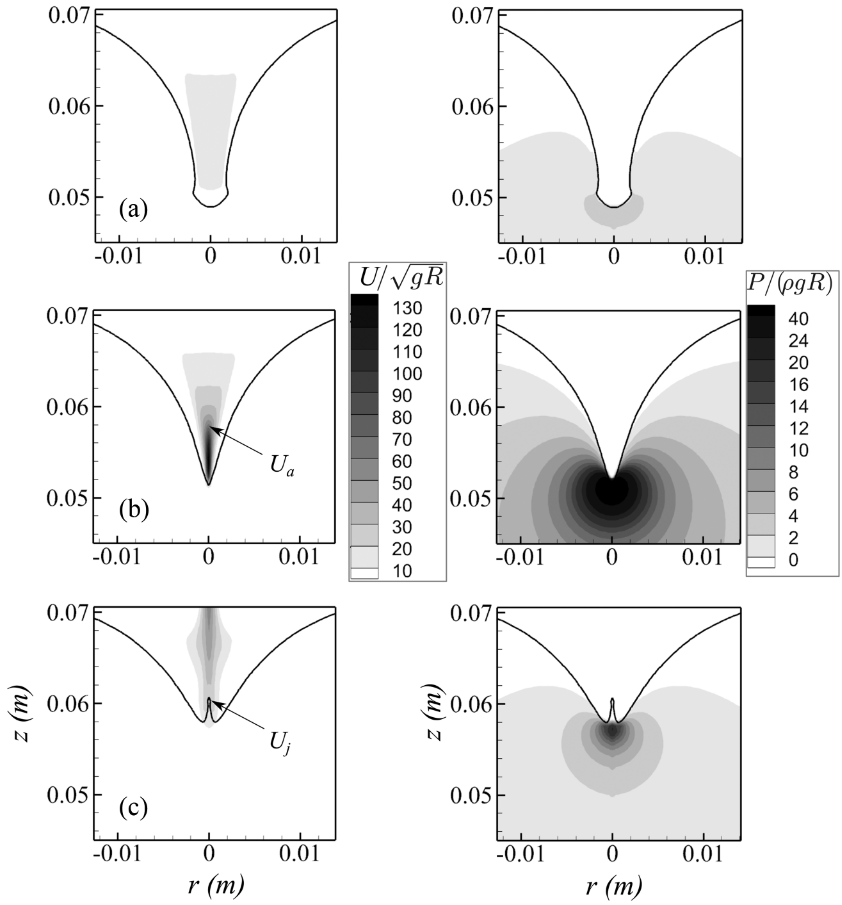

FIG. 12. The contours of dimensionless axial velocity, $U/\sqrt{gR}$ (left column) and dimensionless pressure $P/(\rho gR)$ (right column) for collapsing cavity in GW 90, (a) $\tau = 0.5$ ms, (b) at collapse ($\tau = 0$), and (c) 0.5 ms after collapse. The velocity U gives the liquid jet velocity $U_j \approx 15$ m/s as well as the air velocity, $U_a \approx 90$ m/s.

2. Velocity field and pressure build-up

As in the experiments, the forcing frequency is fixed at $\omega/\omega_0 = 0.995$, and the forcing amplitude is increased until wave breaking followed by wave-depression cavity collapse is observed. Contours of vertical velocity (left panel) and pressure (right panel) are shown at three different times in Fig. 12. Figure 12(a) represents 0.5 ms before singularity and is comparable with Fig. 5(c). Figure 12(b) corresponds to singular collapse $\tau = 0$, where a singularity is formed at the cavity tip with a high-pressure build-up at the tip, reaching $P \approx 500\rho g Z_c$. In the corresponding left panel [Fig. 12(b)], an air jet of velocity $130\sqrt{Rg}$ m/s is formed. This air jet is caused by the pressure build-up at the cavity tip and is not visible in experiments. Such high-speed air jets are also observed in collapse of impact cavities both experimentally (smoke particle imaging) and numerically [26]. The liquid jet velocity in Fig. 12(c) is $U_j \approx 15$ m/s. This value is much less than in experiments (see Fig. 11). The reason is that it was not possible to resolve the singular point properly at $\tau = 0$ because of the extremely small time steps and spatial accuracy needed and of possible numerical viscosity. Nevertheless, it shows qualitatively jet initiation and maximum pressure location. To obtain a jet velocity close to the experimental value, the local pressure impulse would have to be of the order of $10^4 \rho g Z_c$.

[1] R. Bergmann, D. van der Meer, M. Stijnman, M. Sandtke, A. Prosperetti, and D. Lohse, Giant Bubble Pinch-Off, Phys. Rev. Lett. **96**, 154505 (2006).
[2] H. Ding, B. Q. Chen, H. R. Liu, C. Y. Zhang, P. Gao, and X. Y. Lu, On the contact-line pinning in cavity formation during solid–liquid impact, J. Fluid Mech. **783**, 504 (2015).
[3] M. S. Longuet-Higgins, Bubbles, breaking waves and hyperbolic jets at a free surface, J. Fluid Mech. **127**, 103 (1983).
[4] B. W. Zeff, B. Kleber, J. Fineberg, and D. P. Lathrop, Singularity dynamics in curvature collapse and jet eruption on a fluid surface, Nature **403**, 401 (2000).
[5] S. P. Das and E. J. Hopfinger, Parametrically forced gravity waves in a circular cylinder and finite-time singularity, J. Fluid Mech. **599**, 205 (2008).
[6] D. K. Raja, S. P. Das, and E. J. Hopfinger, On standing gravity wave-depression cavity collapse and jetting, J. Fluid Mech. **866**, 112 (2019).
[7] D. K. Raja, S. P. Das, and E. J. Hopfinger, Extreme singular events associated with inertial-viscous cusp formation in fluids, Phys. Fluids **32**, 062104 (2020).
[8] J. M. Boulton-Stone and J. R. Blake, Gas bubbles bursting at a free surface, J. Fluid Mech. **254**, 437 (1993).
[9] F. MacIntyre, Flow patterns in breaking bubbles, J. Geophys. Res. **77**, 5211 (1972).
[10] E. Ghabache, A. Antkowiak, C. Josserand, and T. Séon, On the physics of fizziness: How bubble bursting controls droplets ejection, Phys. Fluids **26**, 121701 (2014).
[11] S. Krishnan, E. J. Hopfinger, and B. A. Puthenveettil, On the scaling of jetting from bubble collapse at a liquid surface, J. Fluid Mech. **822**, 791 (2017).
[12] A. M. Gañán-Calvo, Scaling laws of top jet drop size and speed from bubble bursting including gravity and inviscid limit, Phys. Rev. Fluids **3**, 091601 (2018).
[13] C-Y. Lai, J. Eggers, and L. Deike, Bubble Bursting: Universal Cavity and Jet Profiles, Phys. Rev. Lett. **121**, 144501 (2018).
[14] P. L. L. Walls, L. Henaux, and J. C. Bird, Jet drops from bursting bubbles: How gravity and viscosity couple to inhibit droplet production, Phys. Rev. E. **92**, 021002(R) (2015).
[15] D. Bartolo, C. Josserand, and D. Bonn, Singular Jets and Bubbles in Drop Impact, Phys. Rev. Lett. **96**, 124501 (2006).
[16] S. T. Thoroddsen, K. Takehara, H. D. Nguyen, and T. G. Etoh, Singular jets during the collapse of drop-impact craters, J. Fluid Mech. **848**, R3-1 (2018).
[17] M. S. Longuet-Higgins and H. N. Oguz, Critical jets in surface waves and collapsing cavities, Philos. Trans. R. Soc. Lond. **355**, 625 (1997).
[18] A. S. Ismail, A. M. Gañán-Calvo, J. R. Castrejón-Pita, M. A. Herrada, and A. A. Castrejón-Pita, Controlled cavity collapse: Scaling laws of drop formation, Soft Matter **14**, 7671 (2018).
[19] J. Lu and C. M. Corvalan, Dynamical transitions during the collapse of inertial holes, Sci. Rep. **9**, 14649 (2019).
[20] J. C. Burton and P. Taborek, Role of Dimensionality and Axisymmetry in Fluid Pinch-Off and Coalescence, Phys. Rev. Lett. **98**, 224502 (2007).
[21] D. M. Henderson and J. W. Miles, Single-mode faraday waves in small cylinders, J. Fluid Mech. **213**, 95 (1990).
[22] J. Lighthill, *Waves in Fluids* (Cambridge University Press, Cambridge, UK, 1978).
[23] H. Lamb, *Hydrodynamics*, 6th ed. (Cambridge University Press, Cambridge, UK, 1932).
[24] G. K. Rajan and D. M. Henderson, Linear waves at a surfactant-contaminated interface separating two fluids: Dispersion and dissipation of capillary-gravity waves, Phys. Fluids **30**, 072104 (2018).
[25] V. Duclaux, F. Caillé, C. Duez, C. Ybert, L. Bocquet, and C. Clanet, Dynamics of transient cavities, J. Fluid Mech. **591**, 1 (2007).
[26] S. Gekle, I. R. Peters, J. M. Gordillo, D. van der Meer, and D. Lohse, Supersonic Air Flow Due to Solid-Liquid Impact, Phys. Rev. Lett. **104**, 024501 (2010).